Letter

Robust wavefront dislocations of Friedel oscillations in gapped graphene

Shu-Hui Zhang [1,*,†] Jin Yang,[2,*] Ding-Fu Shao [3] Zhenhua Wu [4] and Wen Yang[2,‡]

[1]*College of Mathematics and Physics, Beijing University of Chemical Technology, Beijing 100029, China*

[2]*Beijing Computational Science Research Center, Beijing 100193, China*

[3]*Department of Physics and Astronomy and Nebraska Center for Materials and Nanoscience, University of Nebraska–Lincoln, Lincoln, Nebraska 68588-0299, USA*

[4]*Key Laboratory of Microelectronics Devices and Integrated Technology, Institute of Microelectronics of Chinese Academy of Sciences, Beijing 100029, China*

(Received 3 January 2021; revised 11 April 2021; accepted 12 April 2021; published 21 April 2021)

Friedel oscillation is a well-known wave phenomenon which represents the oscillatory response of electron waves to imperfection. By utilizing the pseudospin-momentum locking in gapless graphene, two recent experiments demonstrate the measurement of the topological Berry phase by corresponding to the unique number of wavefront dislocations in Friedel oscillations. Here, we study the Friedel oscillations in gapped graphene, in which the pseudospin-momentum locking is broken. Unusually, the wavefront dislocations do occur like that in gapless graphene, which requires immediate verification in the current experimental condition. The number of wavefront dislocations is ascribed to the invariant pseudospin winding number in gapped and gapless graphene. This study deepens the understanding of the correspondence between topological quantity and wavefront dislocations in Friedel oscillations and implies the possibility to observe the wavefront dislocations of Friedel oscillations in intrinsic gapped two-dimensional materials, e.g., transition metal dichalcogenides.

DOI: 10.1103/PhysRevB.103.L161407

Since the seminal discovery of graphene [1], two-dimensional materials have attracted wide interest because of their novel physics and great potential applications [2]. Usually, two-dimensional materials have high mobility, in which the quasiparticles move ballistically and exhibit unconventional quantum tunneling and interference [3–8] . One can intentionally add one or two impurities to form the impurity-design system; this kind of system is charming because it is easily handled theoretically and experimentally, and then it can be regarded as the model system for the exploration of ballistic physics [9]. Experimentally, scanning tunneling microscopy (STM) is a proper tool for an impurity-design system [10]. More interesting, the dimensions of two-dimensional materials are very unique. On the one hand, the bare surface properties of two-dimensional materials are also the bulk properties, in contrast to three-dimensional materials. On the other hand, different from the one-dimensional materials, two-dimensional materials with two-dimensional parameter space are enough to evolve the global topological quantity [11]. Therefore, a surface-sensitive STM measurement is promising to explore the topological physics of impurity-design two-dimensional materials.

Friedel oscillations (FOs) are the quantum interference of electronic wave scattering by the imperfection in crystalline host materials [12]. Recently, STM was demonstrated experimentally to measure the topological Berry phase π of monolayer graphene by counting two wavefront dislocations in FOs, which are induced by the intentional hydrogen adatom [13]. One subsequent experiment shows that for bilayer graphene FOs can exhibit four, two, or zero wavefront dislocations explained by the 2π Berry phase, the specific sublattice positions of the single impurity, and the position of the STM tip [14]. The electronic Berry phase as the intrinsic nature of the wave functions is defined in momentum space, which is responsible for many exotic electronic dynamics such as the index shift of the quantum Hall effect in monolayer graphene [15,16] and bilayer graphene [17], Klein tunneling [3,4], and the weak antilocalization [18]. Probing the Berry phase usually requires the magnetic field [4,15,16,19]. These two experiments not only do not need external magnetic field but also realize the measurement of the Berry phase in real space. However, the two experiments both focus on the gapless cases for graphene and emphasize the relation between the Berry phase and the wavefront dislocation number, leaving the influence of the gap opening on the wavefront dislocations unexplored. Presented in the experimental studies in Refs. [13,14], the pseudospin winding number and the Berry phase are equivalent (inequivalent) in gapless (gapped) graphene, which attracts us to explore the effect of the gap opening on the interference pattern of FOs.

A gap opening in graphene occurs in various different ways, with the substrate coupling being a typical example [20]. Most experiments and devices are performed on the substrate-supported graphene, in which lattice mismatch induced inversion symmetry breaking makes the Berry phase an unquantized multiple of π [21]. As a result, the gap opening should challenge the established correspondence relation

*S.-H.Z. and J.Y. contributed equally to this work.

†shuhuizhang@mail.buct.edu.cn

‡wenyang@csrc.ac.cn

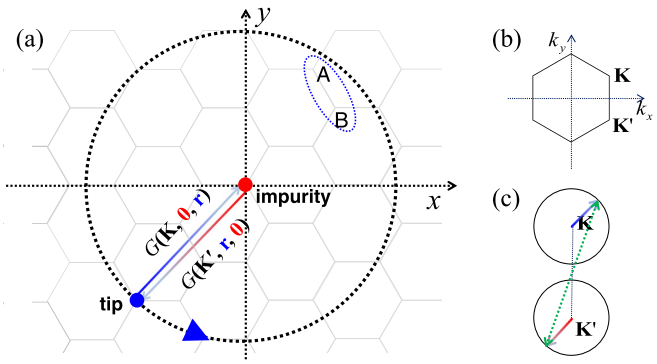

FIG. 1. Schematic measurement of electronic density oscillation by STM. (a) In the real-space atomic structure of graphene, there is a single-atom vacancy (red dot) on one sublattice site; by scanning the STM tip (blue dot) one can probe the vacancy-induced density oscillations which are contributed by the intravalley and intervalley scatterings. Focusing on the intervalley scattering, we plot the corresponding physical process; that is, the STM tip emits the electron waves in one valley $\mathbf{K}$, as shown by the propagator $G(\mathbf{K}, \mathbf{0}, \mathbf{r})$, leading to scattering by the vacancy back to the STM tip through the other valley $\mathbf{K}'$, as shown by the propagator $G(\mathbf{K}', \mathbf{r}, \mathbf{0})$. When the STM tip is shifted around the vacancy in real space as shown by the blue arrow along the circle, the contributing momentum states to the propagator change their momentum around $\mathbf{K}$ and $\mathbf{K}'$, as shown in (c). (b) The Brillouin zone used to define $\mathbf{K}$ and $\mathbf{K}'$. (c) Intervalley scattering (green double arrow) in momentum space. The contributing momentum states in each valley are parallel to $\mathbf{r}$ and are denoted by using the same arrows in (a).

between the Berry phase and the wavefront dislocation number in previous experiments [13,14]. In this study, we study the FOs in gapped graphene. Compared to the gapless graphene, gapped graphene does not have pseudospin-momentum locking, which may prohibit the occurrence of the characteristic interference structure (namely, wavefront dislocations) in FOs following the intuitive picture, as suggested by the seminal work [13]. But the wavefront dislocations in FOs do emerge. Here, we explain the origin of wavefront dislocations by the invariant pseudospin winding number in gapped and gapless graphene, which can be regarded as an updated correspondence relation compatible with previous experiments [13,14]. The wavefront dislocations in FOs of gapped graphene can be verified in the present experimental conditions, and this study helps deepen the understanding of topological physics reflected in the FOs of the impurity-design system.

Figure 1 gives the schematic measurement of the impurity-induced electronic density oscillation of monolayer graphene by STM. The present experimental technology allows one to intentionally introduce a single-atom vacancy on an arbitrary sublattice site of graphene [22], e.g., on sublattice A, as shown by the red dot in Fig. 1(a). Corresponding to the introduction of the single vacancy, FOs occur and lead to the change in the space-resolved and energy-resolved local density of states (LDOS) $\delta\rho(\mathbf{r},\varepsilon)$ [23,24]:

$$\delta\rho(\mathbf{r},\varepsilon) = -\frac{1}{\pi}\,\mathrm{Im}[\mathrm{Tr}\delta\mathbf{G}(\mathbf{r},\mathbf{r},\varepsilon)], \tag{1}$$

where $\delta\mathbf{G} = \mathbf{G} - \mathbf{G}^0$ represents the change in the total Green's function (GF) or propagator $\mathbf{G}$ incorporating the effect of the vacancy relevant to the bare propagator $\mathbf{G}^0$ of the host system [i.e., graphene in Fig. 1(a)] and has the form

$$\delta\mathbf{G}(\mathbf{r}_2,\mathbf{r}_1,\varepsilon) = \mathbf{G}^0(\mathbf{r}_2,\mathbf{0},\varepsilon)\mathbf{T}\mathbf{G}^0(\mathbf{0},\mathbf{r}_1,\varepsilon). \tag{2}$$

Here, the T-matrix approach is used to describe the effect of a vacancy whose potential is simulated by $V_0\delta(\mathbf{r})$, and the T matrix is [25]

$$\mathbf{T}(\varepsilon) = \mathbf{V}[1 - \int d^2\mathbf{k}\mathbf{G}^0(\mathbf{k},\varepsilon)\mathbf{V}]^{-1}. \tag{3}$$

In the T matrix, $\mathbf{V}$ usually is a matrix, and its form depends on the specific position of the vacancy; for example, in Fig. 1(a) (for the other vacancy configuration see the Supplemental Material [26]), it is

$$\mathbf{V} = \begin{bmatrix} V_0 & 0 \\ 0 & 0 \end{bmatrix} \tag{4}$$

using the sublattice basis of $\{A, B\}$. For graphene, there are two Dirac valleys in the Brillouin zone [8] [see Fig. 1(b)], $\mathbf{K} = (\frac{2\pi}{3}, \frac{2\pi}{3\sqrt{3}})$ and $\mathbf{K}' = (\frac{2\pi}{3}, -\frac{2\pi}{3\sqrt{3}})$; then $\delta\rho(\mathbf{r},\varepsilon)$ are contributed by the intravalley and intervalley scatterings. In graphene, the intravalley scattering contribution to $\delta\rho(\mathbf{r},\varepsilon)$ has been well understood through many theoretical [23,25,27–37] and experimental [22,38–41] efforts, while the intervalley scattering contribution has attracted attention very recently due to its underlying topological nature [13,14,42]. $\delta\rho(\mathbf{r},\varepsilon)$ is measured easily by STM. FOs of $\delta\rho(\mathbf{r},\varepsilon)$ are dominated by the backscattering events along the constant-energy contour [43,44]. Focusing on the intervalley scattering, the corresponding physical process of Eq. (2) is shown in Fig. 1(a); that is, the STM tip emits the electron waves from one valley $\mathbf{K}$, as shown by the propagator $G^0(\mathbf{K},\mathbf{0},\mathbf{r},\varepsilon)$, leading to scattering by the vacancy back to the STM tip through the other valley, $\mathbf{K}'$, as shown by the propagator $G^0(\mathbf{K}',\mathbf{r},\mathbf{0},\varepsilon)$. Of course, the conjugate process also exists; that is, the emission (scattering waves) are from the $\mathbf{K}'$ ($\mathbf{K}$) valley. Here, $G^0(\mathbf{K}/\mathbf{K}',\mathbf{0},\mathbf{r},\varepsilon)$ is the matrix element of the 2×2 matrix $\mathbf{G}^0$ and is associated with the valley momentum index $\mathbf{K}/\mathbf{K}'$ for the clear description of intervalley scattering. Then, the arguments of $\mathbf{G}^0$ are increased from ($\mathbf{r}_2$, $\mathbf{r}_1$, ε) to ($\mathbf{K}/\mathbf{K}'$, $\mathbf{r}_2$, $\mathbf{r}_1$, ε), while the position arguments can be abbreviated through $\mathbf{r} = \mathbf{r}_2 - \mathbf{r}_1$ in the uniform graphene as used below. When the STM tip is shifted around the vacancy in real space, as shown in Fig. 1(a), the contributing momentum states to the propagator change their momentum around $\mathbf{K}$ and $\mathbf{K}'$, as shown in Fig. 1(c). As a result, the Berry phase defined in momentum space is measured by STM in real space, and the key is the pseudospin-momentum locking [13]. In contrast, we will show that the pseudospin winding number instead of the Berry phase is measured by STM in gapped graphene without pseudospin-momentum locking.

The physics is essentially the same for gapped monolayer and bilayer graphene, described below using the gapped monolayer as an example; the relevant results for gapped bilayer graphene are given in the Supplemental Material [26]. The Hamiltonian of gapped monolayer graphene is $H_0 = v_F(\eta\sigma_x k_x - \sigma_y k_y) + \Delta\sigma_z$. H_0 is expressed in the sublattice

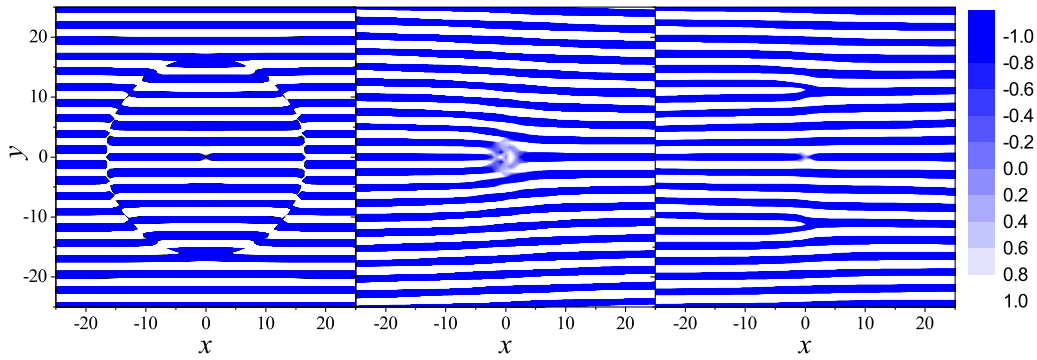

FIG. 2. Friedel oscillation pattern around a single-atom vacancy at the origin. Intervalley scattering contribution to density oscillations $\delta\rho_A(\mathbf{r},\varepsilon)$ and $\delta\rho_B(\mathbf{r},\varepsilon)$ on sublattice A (left panel) and on sublattice B (middle panel), respectively. And the sum $\delta\rho_A(\mathbf{r},\varepsilon)+\delta\rho_B(\mathbf{r},\varepsilon)$ as the total electronic density modulation (right panel). Following Ref. [13], the energy is integrated over energy up to Fermi energy. Here, Fermi level $\varepsilon = 0.11t_0 \simeq 0.4$ eV, $\Delta = 0.017t_0 \simeq 50$ meV, and the color scale is normalized by a numerical factor $C\times 10^{-3}$.

basis of $\{A, B\}$; then $\sigma_{x,y,z}$ is the Pauli matrix acting on the pseudospin space. $\pm\Delta$ is the staggered potential on sublattices A and B, which originates from the inversion symmetry breaking, e.g., from the proximity substrate [20,45]. And $\eta = \pm 1$ is the valley index for two inequivalent valleys in graphene, $v_F = 3/2a_0t_0$, with a_0 being the carbon-carbon bond length and t_0 being the nearest-neighbor hopping energy, where a_0 (t_0) is used as the length (energy) unit in our convention [8]. The energy spectrum and the spinor wave function are, respectively,

$$E_\xi(\mathbf{k}) = \xi v_F\sqrt{\delta^2+k^2} \tag{5}$$

and

$$\psi_{\xi,\mathbf{k}} = \frac{1}{\sqrt{1+k^2/(\epsilon_\xi+\delta)^2}}\begin{bmatrix}1\\ \frac{\eta k_x - ik_y}{\epsilon_\xi+\delta}\end{bmatrix}, \tag{6}$$

where the reduced quantities are defined as $\delta = \Delta/v_F$, $\epsilon_\xi = E_\xi/v_F$, with $\xi = \pm 1$ for the conduction and valence bands. The GF in momentum space is defined as $\mathcal{G}^0(\mathbf{k},\varepsilon) \equiv (z - H_0)^{-1}$, and it is

$$\mathcal{G}^0(\mathbf{k},\varepsilon) = \frac{1}{z^2-\Delta^2-v_F^2k^2}\begin{bmatrix} z+\Delta & \eta v_F k e^{i\eta\theta_k}\\ \eta v_F k e^{-i\eta\theta_k} & z-\Delta\end{bmatrix}. \tag{7}$$

Here, $z = \varepsilon + i0^+$, with 0^+ for the retarded properties of GF, and the Fermi level ε is assumed to be in the conduction band for brevity. Performing the Fourier transformation to the momentum space GF, we express the real-space GF [46] as $\mathbf{G}^{(0)}(\mathbf{K},\mathbf{r},\varepsilon) = -e^{i\mathbf{K}\cdot\mathbf{r}}/(2v_F)^2\mathbf{G}^{(0)}(\mathbf{r},\varepsilon)$, with

$$\mathbf{G}^{(0)}(\mathbf{r},\varepsilon) = \begin{bmatrix} i\varepsilon_+ H_0(u) & \eta\sqrt{\varepsilon_+\varepsilon_-}H_1(u)e^{i\eta\theta_r}\\ \eta\sqrt{\varepsilon_+\varepsilon_-}H_1(u)e^{-i\eta\theta_r} & i\varepsilon_- H_0(u)\end{bmatrix}, \tag{8}$$

where H_j is the jth order Hankel function of the first kind, $\varepsilon_\pm = \varepsilon \pm \Delta$, $u = r\sqrt{\varepsilon_+\varepsilon_-}/v_F$, and r (θ_r) is the module (azimuthal angle) of $\mathbf{r}$. Concentrating on the intervalley contribution, the change in the LDOS is

$$\delta\rho(\delta\mathbf{K},\mathbf{r},\varepsilon) = \delta\rho_A(\mathbf{r},\varepsilon) - \delta\rho_B(\mathbf{r},\varepsilon), \tag{9}$$

where the sublattice-resolved LDOSs are

$$\delta\rho_A(\mathbf{r},\varepsilon) = C\,\mathrm{Im}\left[t(\varepsilon)H_0^2(u)\varepsilon_+^2\right]\cos(\delta\mathbf{K}\cdot\mathbf{r}), \tag{10a}$$

$$\delta\rho_B(\mathbf{r},\varepsilon) = C\,\mathrm{Im}\left[t(\varepsilon)H_1^2(u)\varepsilon_+\varepsilon_-\right]\cos(\delta\mathbf{K}\cdot\mathbf{r} - \delta\eta\theta_r). \tag{10b}$$

Here, $\delta\mathbf{K} = \mathbf{K} - \mathbf{K}'$, $\delta\eta = \eta - \eta'$, $C = 1/(8v_F^4)$, and $t(\varepsilon) = V_0/[1 - V_0G_{AA}^{(0)}(0,\varepsilon)]$ is the matrix element of the T matrix induced by the vacancy on the sublattice A.

Nontrivially, Eq. (9) for the LDOS contributed by the intervalley scattering has a form identical to that in gapless graphene [13], and it reproduces the result of the gapless case when $\Delta \to 0$. For the vacancy on sublattice A, $\delta\rho_A(\mathbf{r},\varepsilon)$ is trivial. $|\delta\eta| = 2$ for the intervalley scattering; then the phase of $\delta\rho_B(\mathbf{r},\varepsilon)$ is singular at $\mathbf{r} = 0$. By shifting the STM tip around the vacancy, i.e., θ_r is rotated by 2π, there should be two additional wavefronts in the FOs pattern of $\delta\rho_B(\mathbf{r},\varepsilon)$ [13]. In Fig. 2, focusing on the intervalley scattering contribution, we show electronic density oscillations around a single-atom vacancy $\delta\rho_A(\mathbf{r},\varepsilon)$ and $\delta\rho_B(\mathbf{r},\varepsilon)$ on sublattice A (left panel) and on sublattice B (middle panel), respectively. The sum $\delta\rho_A(\mathbf{r},\varepsilon)+\delta\rho_B(\mathbf{r},\varepsilon)$ is the total electronic density modulation (right panel). As expected, $\delta\rho_A(\mathbf{r},\varepsilon)$ exhibits the normal oscillating wavefronts perpendicular to $\delta\mathbf{K}$ with a wavelength $\lambda_{\delta\mathbf{K}} = 2\pi/|\delta\mathbf{K}| = 2.60a_0 \approx 3.69$ Å, and does not display any topological feature. $\delta\rho_B(\mathbf{r},\varepsilon)$ gives two wavefront dislocations at $\mathbf{r} = 0$, which accommodates for the phase accumulated along the contour enclosing the singular point of the phase θ_r [47]. In the total electronic density modulation (see the right panel of Fig. 2), $\delta\rho_A(\mathbf{r},\varepsilon)$ only shifts the position of dislocations from $\mathbf{r} = 0$ along the direction parallel to $\delta\mathbf{K}$ and does not change the shape and the number of dislocations [13].

The two additional wavefronts are regarded as the signature of the Berry phase π of graphene. However, the correspondence between the Berry phase and the wavefront dislocation number fails since the Berry phase is an unquantized multiple of π in gapped graphene. Returning to Fig. 1(c), in which we do not follow Refs. [13,14] in plotting the momentum-resolved pseudospin direction, it still shows synchronous

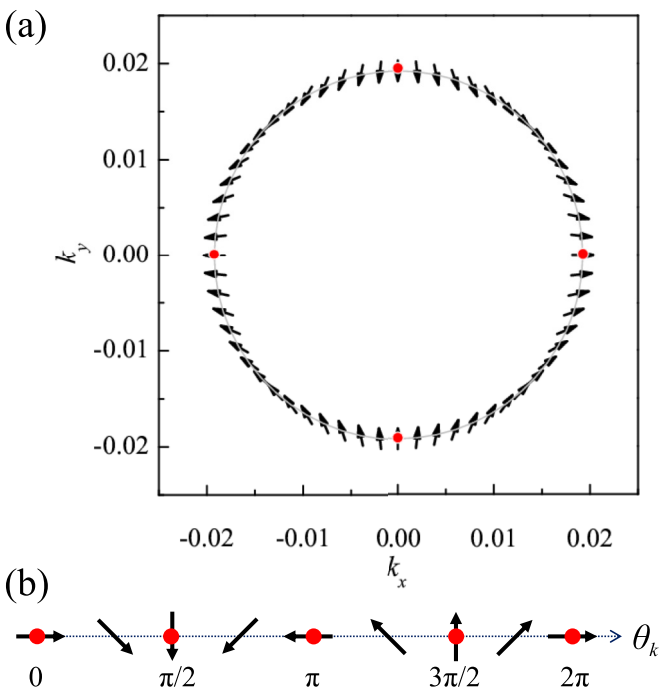

FIG. 3. Pseudospin texture pattern. (a) Pseudospins on the constant-energy contour. (b) Pseudospin as a function of θ_k. Here, $\Delta = 50$ meV, $\varepsilon = 100$ meV, and $\eta = 1$.

motion of the dominant scattering state contributing to FOs in momentum space and the STM tip in real space; for example, the scattering state rotates clockwise (counterclockwise) on the constant-energy contour when the STM tip is shifted clockwise (counterclockwise) around the vacancy. The scattering state can be used to define the pseudospin vector $\mathbf{s} = (s_x, s_y)$, where

$$s_x = \langle \psi_{\xi,\mathbf{k}} | \sigma_x | \psi_{\xi,\mathbf{k}} \rangle = \frac{2\eta k_x(\epsilon_\xi + \delta)}{(\epsilon_\xi + \delta)^2 + k^2}, \tag{11a}$$

$$s_y = \langle \psi_{\xi,\mathbf{k}} | \sigma_y | \psi_{\xi,\mathbf{k}} \rangle = -\frac{2k_y(\epsilon_\xi + \delta)}{(\epsilon_\xi + \delta)^2 + k^2}. \tag{11b}$$

Due to $s_x \sim k_x$ and $s_y \sim k_y$, Eq. (11) gives four fixed points with the momentum azimuthal angle $\theta_k = 0, \pi/2, \pi$, and 2π, at which the pseudospin directions are fixed. This feature has no dependence on δ and thus is robust to the gap opening. To show more visually, we arbitrarily choose a set of parameters to plot the pseudospin texture in Fig. 3. With the scattering state moving on the constant energy contour, the pseudospin direction twists continuously in Fig. 3(a). Clearly, there are four fixed points shown by the red dots [see Fig. 3(a)], which implies the invariant pseudospin winding number. Referring to Fig. 3(b), when θ_k evolves from zero to 2π, the pseudospin rotates by 2π, corresponding to the winding number 1. Alternatively, the invariant pseudospin winding number can also be shown mathematically [48]. We rewrite the gapped Hamiltonian of monolayer graphene into the form

$$H_0(\mathbf{k}) = |E_\xi(\mathbf{k})| \begin{bmatrix} \cos\alpha & \sin\alpha e^{-i\phi} \\ \sin\alpha e^{i\phi} & -\cos\alpha \end{bmatrix}, \tag{12}$$

where the azimuthal $\alpha(\mathbf{k})$ and polar $\phi(\mathbf{k})$ angles on the Bloch sphere are defined as $\cos\alpha = \Delta/|E_\xi(\mathbf{k})|$; $\sin\alpha = |f(\mathbf{k})|/|E_\xi(\mathbf{k})|$, with $f(\mathbf{k}) = v_F(\eta k_x + i k_y)$; and $\phi \equiv -\mathrm{Arg} f$. As a result, we obtain the Berry phase along a closed Fermi surface:

$$\gamma(C) = \oint_C d\mathbf{k} \cdot \mathbf{A}_\xi = \pi W_C \left[1 - \frac{\Delta}{|E_\xi(\mathbf{k})|}\right]. \tag{13}$$

Here, we have used the Berry connection $\mathbf{A}_\xi = i\langle u_{\mathbf{k},\xi} | \nabla_\mathbf{k} u_{\mathbf{k},\xi} \rangle = -\xi \sin^2 \frac{\alpha}{2} \nabla_\mathbf{k} \phi$. Most importantly, the winding number is introduced,

$$W_C \equiv -\xi \oint_C \frac{d\phi}{2\pi} = \eta\xi. \tag{14}$$

While the Berry phase of Eq. (13) has the Δ dependence and becomes an unquantized multiple of π, W_C of Eq. (14) with an absolute value of 1 is topologically invariant in gapless and gapped graphene. As a result, the two wavefront dislocations also exist in gapped graphene, which should be ascribed to the invariant winding number.

Here, we first discuss the experimental implication of our theoretical discovery. When $\Delta \to 0$ for gapless graphene, one can say that the Berry phase and winding number are equivalent; then Berry phase is measured by the wavefront dislocations [13,14]. But a supplementary experiment is necessary to confirm the gapless nature of the graphene sample. In two previous experiments [13,14], there was no such supplementary experiment, and they did not perform the quantitative comparison between experiments and simulations for the FOs, which both prohibit the discovery of the possible gap opening. The quantitative calculations of FOs, especially properly incorporating the strength and range of the impurity potential, are rather important and are worth further simulations, e.g., using density functional calculations [49]. Also, this experimental discussion is also applicable to one recent theoretical proposal, which used the presence or absence of wavefront dislocations in FOs to distinguish the incompatible low-energy models for twisted bilayer graphene [50]. In light of the present experimental technology, we expect immediate verification of our theoretical prediction in gapped graphene. In addition, our results may stimulate theoretical and experimental research interest in the FOs in intrinsic gapped two-dimensional materials, e.g., transition metal dichalcogenides [51,52].

The robustness of the wavefront dislocations of FOs to the gap opening dictates the potential applications in graphene-based pseudospintronics [53]. Each imperfection can be regarded as one vortex, and the sublattice dependence of wavefront dislocation helps define the vortex and antivortex since the orientations of the tripod shape of the imperfection on two sublattices are different [13]. Then, we can use a vortex (antivortex) of 0 (1) to construct the memory device. The writing of a vortex-based memory device can be performed by using STM to shift the imperfection from one sublattice to the other one [22], while its reading is realized by scanning the imperfection-induced FOs to characterize the orientations of the tripod shape of the imperfection. One recent experiment [42] studied the effect of spacing on the wavefront dislocation of two vortices and showed the irrelevant vortices on the several nanometer scale which

favors the high density of a vortex-based memory device. This implies the great potential of impurity-design graphene in pseudospintronics.

In summary, we have studied the Friedel oscillation in gapped graphene. Although the pseudospin-momentum locking is broken, the wavefront dislocations still emerge in Friedel oscillations contributed by intervalley scattering. We establish the correspondence between the invariant winding number instead of the Berry phase and the number of wavefront dislocations in gapped graphene, which can be verified by the present experimental technology. This study is helpful for understanding the correspondence between the topological quantity and wavefront dislocations in Friedel oscillations and broadens the range of materials to observe the wavefront dislocations of Friedel oscillations, e.g., in transition metal dichalcogenides [51,52].

The authors thank Dr. L.-K. Shi for helpful discussions. This work was supported by the National Key R&D Program of China (Grant No. 2017YFA0303400), the National Natural Science Foundation of China (NSFC; Grants No. 11774021 and No. 11504018), and the NSAF grant in NSFC (Grant No. U1930402). We acknowledge the computational support from the Beijing Computational Science Research Center (CSRC).

[1] K. S. Novoselov, A. K. Geim, S. V. Morozov, D. Jiang, Y. Zhang, S. V. Dubonos, I. V. Grigorieva, and A. A. Firsov, Science **306**, 666 (2004).
[2] C. Liu, H. Chen, S. Wang, Q. Liu, Y.-G. Jiang, D. W. Zhang, M. Liu, and P. Zhou, Nat. Nanotechnol. **15**, 545 (2020).
[3] M. I. Katsnelson, K. S. Novoselov, and A. K. Geim, Nat. Phys. **2**, 620 (2006).
[4] A. F. Young and P. Kim, Nat. Phys. **5**, 222 (2009).
[5] V. V. Cheianov, V. Fal'ko, and B. L. Altshuler, Science **315**, 1252 (2007).
[6] C. W. J. Beenakker, R. A. Sepkhanov, A. R. Akhmerov, and J. Tworzydło, Phys. Rev. Lett. **102**, 146804 (2009).
[7] Z. Wu, F. Zhai, F. M. Peeters, H. Q. Xu, and K. Chang, Phys. Rev. Lett. **106**, 176802 (2011).
[8] A. H. Castro Neto, F. Guinea, N. M. R. Peres, K. S. Novoselov, and A. K. Geim, Rev. Mod. Phys. **81**, 109 (2009).
[9] M. Settnes, S. R. Power, D. H. Petersen, and A.-P. Jauho, Phys. Rev. Lett. **112**, 096801 (2014).
[10] D. N. Basov, M. M. Fogler, A. Lanzara, F. Wang, and Y. Zhang, Rev. Mod. Phys. **86**, 959 (2014).
[11] C. Dutreix, M. Bellec, P. Delplace, and F. Mortessagne, arXiv:2006.08556.
[12] J. Friedel, London, Edinburgh, Dublin Philos. Mag. J. Sci. **43**, 153 (1952).
[13] C. Dutreix, H. Gonzalez-Herrero, I. Brihuega, M. I. Katsnelson, C. Chapelier, and V. T. Renard, Nature (London) **574**, 219 (2019).
[14] Y. Zhang, Y. Su, and L. He, Phys. Rev. Lett. **125**, 116804 (2020).
[15] K. S. Novoselov, A. K. Geim, S. V. Morozov, D. Jiang, M. I. Katsnelson, I. V. Grigorieva, S. V. Dubonos, and A. A. Firsov, Nature (London) **438**, 197 (2005).
[16] Y. Zhang, Y.-W. Tan, H. L. Stormer, and P. Kim, Nature (London) **438**, 201 (2005).
[17] K. S. Novoselov, E. McCann, S. V. Morozov, V. I. Fal'ko, M. I. Katsnelson, U. Zeitler, D. Jiang, F. Schedin, and A. K. Geim, Nat. Phys. **2**, 177 (2006).
[18] X. Wu, X. Li, Z. Song, C. Berger, and W. A. de Heer, Phys. Rev. Lett. **98**, 136801 (2007).
[19] D. Xiao, M.-C. Chang, and Q. Niu, Rev. Mod. Phys. **82**, 1959 (2010).
[20] A. Chaves, J. G. Azadani, H. Alsalman, D. R. da Costa, R. Frisenda, A. J. Chaves, S. H. Song, Y. D. Kim, D. He, J. Zhou, A. Castellanos-Gomez, F. M. Peeters, Z. Liu, C. L. Hinkle, S.-H. Oh, P. D. Ye, S. J. Koester, Y. H. Lee, Ph. Avouris, X. Wang, and T. Low, npj 2D Mater. Appl. **4**, 29 (2020).
[21] W. Yao, D. Xiao, and Q. Niu, Phys. Rev. B **77**, 235406 (2008).
[22] H. González-Herrero, J. M. Gómez-Rodríguez, P. Mallet, M. Moaied, J. J. Palacios, C. Salgado, M. M. Ugeda, J.-Y. Veuillen, F. Yndurain, and I. Brihuega, Science **352**, 437 (2016).
[23] C. Bena, Phys. Rev. Lett. **100**, 076601 (2008).
[24] Y.-L. Zou, J. Song, C. Bai, and K. Chang, Phys. Rev. B **94**, 035431 (2016).
[25] C. Dutreix and M. I. Katsnelson, Phys. Rev. B **93**, 035413 (2016).
[26] See Supplemental Material at http://link.aps.org/supplemental/10.1103/PhysRevB.103.L161407 for the derivations of the Green's function and Friedel oscillations in gapped monolayer and bilayer graphene.
[27] V. V. Cheianov and V. I. Fal'ko, Phys. Rev. Lett. **97**, 226801 (2006).
[28] E. H. Hwang and S. Das Sarma, Phys. Rev. Lett. **101**, 156802 (2008).
[29] T. Pereg-Barnea and A. H. MacDonald, Phys. Rev. B **78**, 014201 (2008).
[30] C. Bena, Phys. Rev. B **79**, 125427 (2009).
[31] F. M. D. Pellegrino, G. G. N. Angilella, and R. Pucci, Phys. Rev. B **80**, 094203 (2009).
[32] A. Bácsi and A. Virosztek, Phys. Rev. B **82**, 193405 (2010).
[33] G. Gómez-Santos and T. Stauber, Phys. Rev. Lett. **106**, 045504 (2011).
[34] J. A. Lawlor, S. R. Power, and M. S. Ferreira, Phys. Rev. B **88**, 205416 (2013).
[35] M. Settnes, S. R. Power, D. H. Petersen, and A.-P. Jauho, Phys. Rev. B **90**, 035440 (2014).
[36] M. Settnes, S. R. Power, J. Lin, D. H. Petersen, and A.-P. Jauho, Phys. Rev. B **91**, 125408 (2015).
[37] T. M. Rusin and W. Zawadzki, Phys. Rev. B **97**, 205410 (2018).
[38] G. M. Rutter, J. N. Crain, N. P. Guisinger, T. Li, P. N. First, and J. A. Stroscio, Science **317**, 219 (2007).
[39] I. Brihuega, P. Mallet, C. Bena, S. Bose, C. Michaelis, L. Vitali, F. Varchon, L. Magaud, K. Kern, and J. Y. Veuillen, Phys. Rev. Lett. **101**, 206802 (2008).
[40] P. Mallet, I. Brihuega, S. Bose, M. M. Ugeda, J. M. Gómez-Rodríguez, K. Kern, and J. Y. Veuillen, Phys. Rev. B **86**, 045444 (2012).
[41] K. W. Clark, X.-G. Zhang, G. Gu, J. Park, G. He, R. M. Feenstra, and A.-P. Li, Phys. Rev. X **4**, 011021 (2014).

[42] Y. Zhang, Y. Su, and L. He, Nano Lett. **21**, 2526 (2021).
[43] P. T. Sprunger, L. Petersen, E. W. Plummer, E. Laegsgaard, and F. Besenbacher, Science **275**, 1764 (1997).
[44] S.-H. Zhang, D.-F. Shao, and W. Yang, J. Magn. Magn. Mater. **491**, 165631 (2019).
[45] S. Y. Zhou, G.-H. Gweon, A. V. Fedorov, P. N. First, W. A. de Heer, D.-H. Lee, F. Guinea, A. H. Castro Neto, and A. Lanzara, Nat. Mater. **6**, 770 (2007).
[46] J.-J. Zhu, D.-X. Yao, S.-C. Zhang, and K. Chang, Phys. Rev. Lett. **106**, 097201 (2011).
[47] J. F. Nye, M. V. Berry, and F. C. Frank, Proc. R. Soc. London, Ser. A **336**, 165 (1974).
[48] J. N. Fuchs, F. Piéchon, M. O. Goerbig, and G. Montambaux, Eur. Phys. J. B **77**, 351 (2010).
[49] K. Noori, S. Y. Quek, and A. Rodin, Phys. Rev. B **102**, 195416 (2020).
[50] V. O. T. Phong and E. J. Mele, Phys. Rev. Lett. **125**, 176404 (2020).
[51] Q. H. Wang, K. Kalantar-Zadeh, A. Kis, J. N. Coleman, and M. S. Strano, Nat. Nanotechnol. **7**, 699 (2012).
[52] J. R. Schaibley, H. Yu, G. Clark, P. Rivera, J. S. Ross, K. L. Seyler, W. Yao, and X. Xu, Nat. Rev. Mater. **1**, 16055 (2016).
[53] D. Pesin and A. H. MacDonald, Nat. Mater. **11**, 409 (2012).